Computational evaluation of the reactivity and pharmaceutical potential of an organic amine: A DFT, molecular dynamics simulations and molecular docking approach

Christina Susan Abraham [a], S. Muthu [b,*], Johanan Christian Prasana [a], Stevan Armaković [c], Sanja J. Armaković [d], Fathima Rizwana B. [a], Ben Geoffrey [a], Host Antony David R. [e]

[a] Department of Physics, Madras Christian College, East Tambaram 600059, Tamil Nadu, India
[b] Department of Physics, Arignar Anna Government Arts College, Cheyyar 604407, Tamil Nadu, India
[c] University of Novi Sad, Faculty of Sciences, Department of Physics, Trg D. Obradovića 4, 21000 Novi Sad, Serbia
[d] University of Novi Sad, Faculty of Sciences, Department of Chemistry, Biochemistry and Environmental Protection, Trg D. Obradovića 3, 21000 Novi Sad, Serbia
[e] Bioinformatics center of BITSnet, Madras Christian College, East Tambaram 600059, Tamil Nadu, India

ARTICLE INFO

ABSTRACT

2-[N-(carboxymethyl)anilino] acetic acid (PIDAA) molecule has been spectroscopically characterized and computationally investigated for its fundamental reactive properties by a combination of density functional theory (DFT) calculations, molecular dynamics (MD) simulations and molecular docking procedure. A comparison drawn between the simulated and experimentally attained spectra by FT-Raman and FT-IR showed concurrence. The natural bond orbital (NBO) analysis enabled in comprehending the stability and charge delocalization in the title molecule. The first hyperpolarizability which is an important parameter for future studies of nonlinear optics (NLO) was calculated to check the potential of the molecule to be an NLO material. Besides, frontier molecular orbitals (FMO), electron localization function (ELF) and localized orbital locator (LOL) analysis were performed. Energy gap (ΔE), electronegativity (χ), chemical potential (μ), global hardness (η), softness (S), Mulliken population analysis on atomic charges and thermodynamic properties of the title compound at different temperatures have been calculated. The local reactive properties of PIDAA have been addressed by MEP and ALIE surfaces, together with bond dissociation energy for hydrogen abstraction (H-BDE). MD simulations have been used in order to identify atoms with pronounced interactions with water molecules. The pharmaceutical potential of PIDAA has been considered by the analysis of drug likeness parameters and molecular docking procedure. The biological activity of the molecule in terms of molecular docking has been analyzed theoretically for the treatment of SARS and minimum binding energy calculated. The Ramachandran plot was used to check the stereochemistry of the protein structure. In addition, a comparison of the physiochemical parameters of PIDAA and commercially available drugs (Yu et al., 2004; Tan et al., 2004; Elshabrawy et al., 2014; Chu et al., 2004; Gopal Samy and Xavier, 2015) were carried out.

© 2019 Elsevier B.V. All rights reserved.

1. Introduction

2-[N-(carboxymethyl)anilino] acetic acid, with two symmetrically situated carboxylic acid groups (polyamino carboxylic acid), is a surface-active tertiary aryl amine. The presence of its iminodiacetic acid structure makes it acidic ($pK_1 = 2.5$) in nature. With two fused, five membered chelate rings the iminodiacetate anion can act as a tridentate ligand to form a metal complex [6]. It also is an important entity to carry out the hepatobiliary (HIDA) scan which is an imaging technique used to detect problems of the liver.

PIDAA, in particular, has various applications associated with it. By the acid-amine complexation mechanism, PIDAA acid is expected to be proficient in triggering the polymerization of carboxylic acid monomers [7,8]. The tertiary aryl amine structure of PIDAA makes it a prospective photochemical and chemical polymerization accelerator. By employing a diazotation reaction phenyl-iminodiacetic acid groups were covalently grafted onto multi-walled carbon nanotubes and it behaved as a valuable solid-phase extraction [9]. In addition, it is also used for Serve Acute Respiratory Syndrome Treatment (SARS). SARS is a viral respiratory disease caused by the SARS coronavirus (SARS-CoV) which leads to upper-respiratory tract illnesses [10,11]. Theoretically, it was found that PIDAA docks itself to the crystal structure of human Angiotensin converting enzyme 4APH [12] and behaves as a possible

* Corresponding author.
E-mail address: mutgee@gmail.com (S. Muthu).

treatment for SARS. Organic molecules that have the ability to act as pharmaceutical drugs can be analyzed for their relationship between structural and biological parameters. This can be devised by correlating the biological activity of the selected compounds with computable physiochemical parameters [13].

In view of these significant distinctions, the present work proposes to fully scrutinize the biological characterization of PIDAA along with the DFT calculations to investigate molecular geometry, electronic structure and chemical bond interactions. Computational characterization of the title molecule in terms of B3LYP provides an elaborate understanding of various properties of PIDAA. Dunning's basis set (aug-cc-pVDZ) has also been chosen apart from the regular basis set and implemented in various DFT methods. Computational techniques within the frameworks of DFT calculations and MD simulations provide outstanding tools for complementing experimental findings and understanding the reactivity of various molecular structures [14–17]. Various scientific and industrial areas rely on the efficiency of computational molecular modeling techniques [18–22].

2. Experimental and theoretical methods

2.1. Physiochemical measurements

The title compound 2-[N-(carboxymethyl)anilino]acetic acid ($C_{10}H_{11}NO_4$) in the solid form was procured from the Alfa Aesar Chemical Company, (USA) and used without further purification for the spectral measurements. The Fourier transform infrared (FT-IR) spectrum of the compound was recorded in the region 4000–450 cm^{-1} using Spectrum one: FT-IR Spectrometer equipped with a KBr beam splitter. The FT-Raman spectrum was recorded on Bruker RFS 27: Stand-alone FT-Raman spectrometer using a 1064-nm line of a Nd:YAG laser source as the excitation source in the region 4000–100 cm^{-1} at the Sophisticated Analytical Instrumentation Facility (SAIF), IIT, Chennai, India. The ultraviolet absorption spectrum of the sample was examined in the range 200–800 nm using Lambda 35 UV Winlab Spectrometer.

2.2. Theoretical methodology

Quantum chemical calculations in this work were carried out using Gaussian 09 W software package [23]. Employing the Becke–Lee–Yang–Parr functional (B3LYP) method [24] with 6-311++G(d,p) basis set, the structure of PIDAA was optimized using density functional theory (DFT). For all of the spectroscopic, molecular docking and physicochemical calculations, such as frontier molecular orbitals, molecular electrostatic potential map (MEP), thermodynamic and nonlinear optical properties in this study the optimized structural parameters were used.

The harmonic vibrational frequencies obtained calculations were scaled by 0.96 above 3000 cm^{-1} and 0.961 below 3000 cm^{-1} ranges, respectively. Using VEDA 4 program [25] the theoretical vibrational assignments was allotted by means of PEDs. The chemical bonding between the atoms of PIDAA was studied in terms of ELF and LOL [26]. The electronic absorption spectrum was calculated using the time-dependent density functional theory (TD-DFT) in DMSO solution. The orbital contribution was analyzed using GaussSum software [27] and the optimized structure was docked using AutoDock Tools (ADT) Version 1.5.6 [28].

Schrödinger Materials Science Suite 2018-1 has been applied as well, for the computational study of title molecule. Particularly, Jaguar [29–31], Desmond [32–35] and Maestro [36] programs preparation and visualization of results of the studied molecule. Same as in the case of Gaussian 09 W, a B3LYP exchange-correlation functional [37] has been used, together with 6-311++G(d,p) basis set for calculations of molecular electrostatic potential (MEP) and average local ionization energy (ALIE) surfaces. For calculations of bond dissociation energies for hydrogen abstraction (H-BDE), a 6-311G(d,p) basis set was used.

Table 1
Optimized geometrical parameters of PIDAA: bond length (Å) and bond angles (°).

Parameter	Experimental	B3LYP/6-311++G(d,p)
Bond length (Å)		
N1-C2	1.399	1.359
N1-C9	1.351	1.467
N1-C13	1.501	1.463
C2-C3	1.409	1.432
C2-C7	1.394	1.433
C3-C4	1.387	1.375
C3-H16	–	1.08
C4-C5	1.365	1.406
C4-H17	0.9802	1.083
C5-C6	1.38	1.406
C5-H18	1.0375	1.083
C6-C7	1.394	1.375
C6-H19	1.0097	1.083
C7-H20	1.025	1.081
C8-C9	1.504	1.539
C8-O10	1.200	1.196
C8-O11	1.412	1.344
C9-H21	–	1.091
C9-H22	–	1.085
O11-H23	0.8986	0.972
C12-C13	1.496	1.535
C12-O14	1.200	1.199
C12-O15	1.303	1.335
Bond angle (°)		
C2-N1-C9	129.6	121.4
C2-N1-C13	–	122.7
N1-C2-C3	119.5	120.9
N1-C2-C7	121.7	120.4
C9-N1-C13	112.1	115.8
N1-C9-C8	114.5	113.3
N1-C9-H21	–	107.8
N1-C9-H22	–	110.6
N1-C13-C12	111.2	111.3
N1-C13-H24	–	108.2
N1-C13-H25	–	111.2
C3-C2-C7	118.8	118.6
C2-C3-C4	118.7	120.1
C2-C3-H16	119.7	120.7
C2-C7-C6	120.5	120.1
C2-C7-H20	120.4	120.7
C4-C3-H16	–	119.1
C3-C4-C5	122.1	120.5
C3-C4-H17	–	119.6
C5-C4-H17	–	119.9
C4-C5-C6	118.8	120.1
C4-C5-H18	119.7	119.9
C6-C5-H18	–	120
C5-C6-C7	121.1	120.5
C5-C6-H19	117.8	119.9
C7-C6-H19	120.6	119.5
C6-C7-H20	119	119.2
C9-C8-O10	122.5	123.3
C9-C8-O11	113.3	111
C8-C9-H21	–	108.4
C8-C9-H22	–	108.8
O10-C8-O11	125.5	125.7
C8-O11-H23	–	109.2
H21-C9-H22	–	107.7
C13-C12-O14	124.1	124.3
C13-C12-O15	109.8	109.4
C12-C13-H24	–	109.1
C12-C13-H25	–	110.5
O14-C12-O15	126.0	126.3
C12-O15-H26	–	109.4
Dihedral angle (°)		
N1-C2-C3-C4	176.6	177.8
N1-C2-C7-C6	−177.3	−178.9
N1-C13-C12-O15	177.3	178.2
N1-C9-C8-O11	176.4	173.2

MD simulations have been performed by using the OPLS3 force field [32,38–40]. Simulation time was set to 10 ns, temperature to 300 K, the pressure to 1.0325 bar and cut-off radius to 12 Å. The modeling of MD systems was performed by placing the one molecule of PIDAA to the simulation box with around 3000 water molecules. The system was considered as isothermal–isobaric (NPT) ensemble, while the simple point charge (SPC) model [35] was used for the treatment of solvent. Maestro program was used for calculations of drug likeness parameters. Drug likeness parameters have been calculated for PIDAA, in order to evaluate its pharmaceutical potential. Frequently used drug likeness parameters in this study encompassed: number of rotatable bonds, hydrogen bond donors and acceptors (HBD and HBA, respectively), AlogP, polar surface area (PSA) and molar refractivity.

3. Results and discussions

The optimization convergence graph as seen in Fig. S1 shows that stable minimum energy was attained thereby showing that the structure of the title molecule considered for all the quantum computational calculations in this section is in the most stable completely optimized state.

3.1. Geometrical optimization

Optimized structural parameters in terms of the bond distance and bond angles are presented in Table 1 in accordance with the atom numbering scheme given in Fig. 1. The optimized geometry of the studied compound had a final geometric energy = −743.573 au and was compared with the structural parameters obtained from the crystallographic information file (CIF) of a similar molecule [41,42]. The C=O bond length was theoretically measured as 1.196 and 1.199 Å, which lie within the standard range 1.196–1.211 Å [43]. The presence of the adjacent O and N atoms leads to lone-pair-lone-pair repulsions thus, the bond lengths C8-C9 and C12-C13 are 1.538 Å and 1.535 Å are slightly shorter than the typical C—C bonds. N1-C2, N1-C9 and N1-C13 are abbreviated from the normal value (1.47 Å) [44]. The CC bonds (1.54 Å) are longer in comparison to the CH bonds (1.1 Å) due to the interaction between the N1 lone pair of electrons and the delocalized electrons in the ring [45].

Phenyl ring is found to be planar within 1° twist. Asymmetry of phenyl ring angles is evidence for deviation of *exo*-angles C7-C2-N1 and C3-C2-N1 which are 121.7° (120.4°) and 119.5° (120.9°). Deviation of angles from the normal value 120° is due to the presence of hyperconjugative interaction. The torsion angles N-C(13)-C(12)-O(15) and N-C(9)-C(8)-O(11) with value −1.8° and −3.6° indicate that the glycinato arms are almost planar. To increase the strain in the glycinato arms they can be coordinated.

Fig. 1. Optimized geometric structure with atom numbering of PIDAA.

Table 2
Second order perturbation theory analysis of Fock matrix in NBO basis of PIDAA.

Donor	Type	ED/e	Acceptor	Type	ED/e	E(2)[a] kcal/mol	E(j)-E(i)[b] a.u.	F(i,j)[c] a.u.
NI-C2	σ	1.98401	N1-C9	σ*	0.0257	0.66	1.07	0.024
			N1-C13	σ*	0.02171	0.63	1.06	0.023
N1-C9	σ	1.97765	N1-C2	σ*	0.03424	1.16	1.09	0.032
N1-C13	σ	1.98318	N1-C2	σ*	0.02282	0.93	1.1	0.029
C2-C3	σ	1.97598	C6-C7	π*	0.32784	18.42	0.28	0.064
			C4-C5	π*	0.3442	20.61	0.27	0.067
C3-C4	σ	1.97875	N1-C2	σ*	0.03424	4.04	1.06	0.059
			C2-C7	σ*	0.0272	4.75	1.06	0.063
			C4-C5	σ*	0.01438	3.41	1.06	0.054
C4-C5	π	1.67086	C2-C3	π*	0.36503	18.3	0.27	0.063
			C6-C7	π*	0.32784	20.14	0.27	0.066
C4-H17	σ	1.98166	C2-C3	σ*	0.02714	3.65	1.06	0.056
			C5-C6	σ*	0.01439	3.6	1.06	0.055
C5-H18	σ	1.98116	C3-C4	σ*	0.01374	3.7	1.05	0.056
			C6-C7	σ*	0.01343	3.68	1.06	0.056
C6-C7	σ	1.97869	N1-C2	σ*	0.03424	4.05	1.06	0.059
C6-C7	π	1.67098	C2-C3	π*	0.36503	21.46	0.27	0.069
			C4-C5	π*	0.3442	19	0.27	0.064
C9-H21	σ	1.97274	N1-C2	σ*	0.03424	4.39	0.87	0.055
			C8-O11	σ*	0.09936	4.05	0.87	0.054
C9-H22	σ	1.97209	N1-C13	σ*	0.02171	2.66	0.83	0.042
			C8-O10	σ*	0.02282	2.34	1.12	0.046
			C8-O10	π*	0.02282	3.94	0.51	0.042
O11-H23	σ	1.98478	C8-C9	σ*	0.06965	3.91	1.13	0.06
C12-C13	σ	1.97759	N1-C2	σ*	0.03424	3.1	1.06	0.051
C13-H24	σ	1.96648	C12-O14	π*	0.22256	4.77	0.51	0.046
C13-H25	σ	1.96553	N1-C9	σ*	0.0257	2.62	0.88	0.043
			C12-O14	σ*	0.02335	2.14	1.12	0.044
			C12-O14	π*	0.22256	5.06	0.51	0.047
O15-H26	σ	1.98514	C12-C13	σ*	0.0613	3.94	1.13	0.06
N1	LP(1)	1.85254	C2-C3	σ*	0.02714	4.82	0.78	0.056
			C2-C3	π*	0.36503	7.92	0.26	0.043
			C2-C7	σ*	0.0272	4.71	0.78	0.056
			C8-C9	σ*	0.06965	6.01	0.62	0.056
			C9-H22	σ*	0.02586	5.7	0.61	0.054
			C13-H24	σ*	0.02175	6.27	0.59	0.056
			C13-H25	σ*	0.02184	6.12	0.59	0.055
O10	LP(2)	1.85513	C8-C9	σ*	0.06965	17.29	0.65	0.097
			C8-O11	σ*	0.09936	32.98	0.64	0.131
O11	LP(1)	1.97212	C8-O10	σ*	0.02282	7.28	1.26	0.086
			C8-O10	π*	0.02282	46.68	0.36	0.116
O14	LP(1)	1.96231	C9-H21	σ*	0.04016	9.44	1.16	0.093
O14	LP(2)	1.83576	C9-H21	σ*	0.04016	12.48	0.75	0.089
			C12-C13	σ*	0.0613	15.49	0.67	0.093
			C12-O15	σ*	0.08928	32.26	0.65	0.131
O15	LP(1)	1.97515	C12-O14	σ*	0.02335	7.36	1.25	0.086
O15	LP(2)	1.81265	C12-O14	π*	0.22256	48.65	0.35	0.117

[a] E(2) means energy of hyper conjugative interaction (stabilization energy).
[b] E(j) – E(i) is the energy difference between donor i and acceptor j.
[c] F(i,j) is the Fock matrix element between i and j NBO orbital's.

Table 3
Mulliken charge distribution and local softness of PIDAA.

Atom	Mulliken atomic charges			Local softness		
	0, 1 (N)	N + 1 (−1, 2)	N-1 (1,2)	sr⁺ fr⁺	sr⁻ fr⁻	sr⁰ fr⁰
1 N	0.333	0.515	0.485	0.038	−0.032	0.003
2 C	−0.534	−1.871	−0.537	−0.280	0.001	−0.139
3 C	−0.117	−0.056	−0.048	0.013	−0.014	−0.001
4 C	−0.542	0.201	−0.533	0.155	−0.002	0.077
5 C	−0.241	1.028	−0.192	0.265	−0.010	0.128
6 C	−0.241	0.292	−0.221	0.111	−0.004	0.054
7 C	0.249	−0.952	0.283	−0.251	−0.007	−0.129
8 C	0.266	0.549	0.277	0.059	−0.002	0.029
9 C	−0.635	−0.002	−0.707	0.132	0.015	0.074
10 O	−0.269	−0.306	−0.167	−0.008	−0.021	−0.015
11 O	−0.130	−0.113	−0.119	0.004	−0.002	0.001
12 C	0.121	−0.247	0.131	−0.077	−0.002	−0.040
13 C	−0.135	2.280	−0.203	0.505	0.014	0.260
14 O	−0.240	−0.199	−0.201	0.009	−0.008	0.000
15 O	−0.129	−0.185	−0.108	−0.012	−0.004	−0.008
16 H	0.146	−0.194	0.194	−0.071	−0.010	−0.041
17 H	0.179	−0.379	0.239	−0.117	−0.013	−0.065
18 H	0.156	−0.195	0.222	−0.073	−0.014	−0.044
19 H	0.184	−0.274	0.245	−0.096	−0.013	−0.054
20 H	0.145	−0.219	0.190	−0.076	−0.009	−0.043
21 H	0.281	0.285	0.329	0.001	−0.010	−0.005
22 H	0.154	0.083	0.244	−0.015	−0.019	−0.017
23 H	0.290	0.130	0.326	−0.033	−0.008	−0.021
24 H	0.203	−0.086	0.266	−0.061	−0.013	−0.037
25 H	0.212	−0.230	0.283	−0.093	−0.015	−0.054
26 H	0.292	−0.855	0.323	−0.240	−0.006	−0.123

3.2. Natural bond orbital analysis

The electron transfers from filled bonding orbital (donor) to empty antibonding orbitals (acceptor) [46–48] leading to hyperconjugative interactions can be examined by employing the NBO analysis. The donor–acceptor interactions in the NBO basis were evaluated using the second-order Fock matrix [49–51]. The intensive interaction between electron-donors and electron-acceptors is a result of the larger $E(2)$ value leading to a greater extent of conjugation of the whole system. The possible intensive interactions and the perturbation energies are given in Table 2.

In the title molecule, π (C2-C3) → π*(C4-C5) and π*(C6-C7) has 20.61 and 18.42 kJ/mol, π (C4-C5) → π*(C2-C3) and π*(C6-C7) has 18.3 and 20.14 kJ/mol and π (C6-C7) → π*(C2-C3) and π*(C4-C5) has 21.46 and 19 kJ/mol hence they give stronger stabilization to the structure. The stabilization of some part of the ring is due to the intra-

molecular hyper conjugation interaction of the σ and the π electrons of C—C to the anti C—C bond in the ring leads to as evident from Table 2. All these transitions with stabilization energies are corresponding to only three pairs of orbitals, namely (C2-C3), (C4-C5) and (C6-C7) which take place both in forward and backward directions among the orbitals within the ring structure. The interaction energy related to the resonance in the molecule is calculated on the basis of the electron donating from LP(2)O15 → π* (C12-O14) which shows the maximum stabilization of 48.65 kJ/mol.

3.3. Natural atomic orbital and natural hybrid orbital analysis

The natural hybrid orbitals (NHOs) which is derived from the natural atomic orbital (NAO) centered on a particular atom through a unitary transformation result from a symmetrically orthogonalized hybrid orbital [52].

Table S1 lists the unique label of the NBO, natural atomic hybrids h_A and h_B of which the NBO is composed, the sp-hybridization (percentage s-character, p-character, etc.) and the polarization coefficient c_A and c_B of the atomic hybrids. The σ (N1-C2) bond is formed from a $sp^{2.72}$ hybrid of carbon (which is the mixture of 26.83% of s and 73.07% of p atomic orbitals) and a $sp^{2.08}$ hybrid of nitrogen (which is the mixture of 32.42% of s and 67.54% of p atomic orbitals). The higher electronegativity of the N1 atom is reflected in the larger polarization coefficient, c_A (0.785) for the N1 hybrid. This can be expressed as,

$$\sigma_{CC} = 0.785 \, (sp^{2.08})_{N1} + 0.6195 (sp^{2.72})_{C2}$$

The bending of the bond is attained which is then expressed as the deviation angle between these two directions. Carbon of σCC is bent away from the line of C2–C7 centers by 1.6° in hybrid 1 and 1.3° in hybrid 2. Similarly, a little lower bending effect of 1.1° is also noticed at the C6–C7 in hybrid 1 and 1° in hybrid 2. The direction of geometry changes due to the geometrical optimization can be predicted using the data attained from Table S2.

3.4. Charge analysis

The atomic charges of the PIDAA were calculated by natural population analysis (NPA). The Mulliken charges calculated at the B3LYP/6-311 ++G(d,p) basis set are listed in Table 3 and represented graphically in Fig. 2. All oxygen atoms have a negative charge, out of which O10 atom shows the highest value of −0.269 e. This is mainly due to the polar
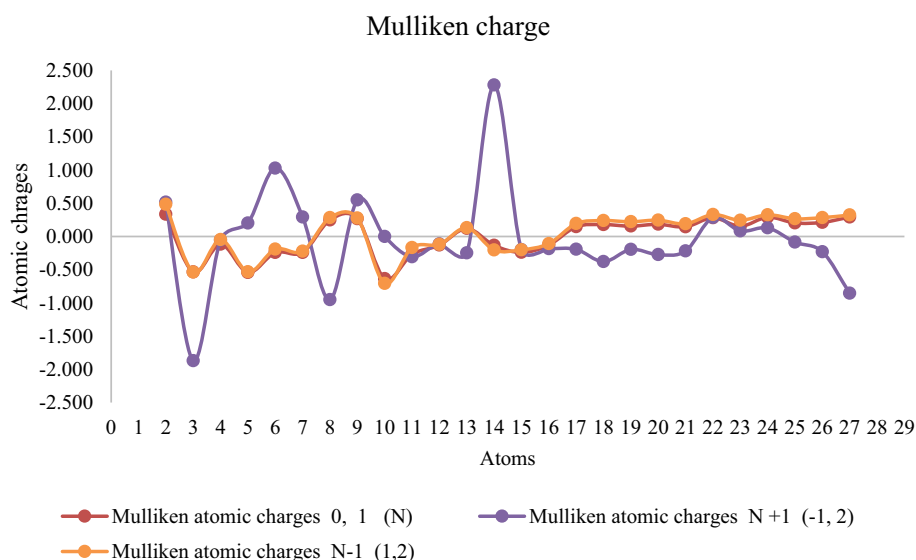
Mulliken charge

Fig. 2. The calculated Mulliken charge of PIDAA.

MEP

ALIE

−29.21 MEP [kcal/mol] 52.01

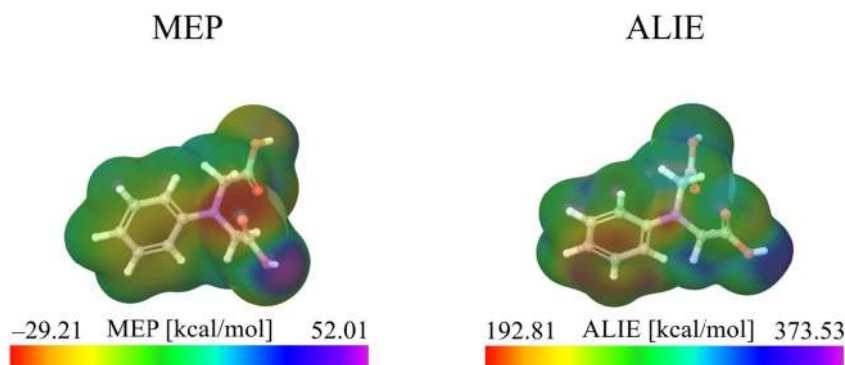192.81 ALIE [kcal/mol] 373.53

Fig. 3. MEP and ALIE surfaces of PIDAA.

nature of carbonyl group and its participation in C-H…O hydrogen bonding interactions. The carbon atoms C7, C8 and C12 acquire positive charge while other carbon atoms of the molecule have a negative charge. Among carbon atoms, C8 possesses the highest positive value (0.266e) and C9 possesses the highest negative value (−0.635e). The highest positive charge on C8 is mainly due to its attachment with two adjacent electronegative oxygen atoms and resonance behavior within COOH group. The highest negative charge on C9 is due to its attachment with the highly electropositive C8 atom. All hydrogen atoms of the molecule are positively charged out of which H26 (0.292 e) has the highest charge. The nitrogen atom of the amino group is found to possess negative value.

3.5. Local reactivity descriptors: MEP and ALIE surfaces

Local reactivity properties of the studied molecule have been firstly addressed by the MEP and ALIE quantities, which are frequently used quantum-molecular descriptors visualized by their mapping to the electron density surface [18,53–60]. MEP surface indicates the abundance or the excess of electrons at certain molecular sites, while ALIE surface indicates molecular sites where electrons require the lowest amount of energy to be removed. ALIE is defined as the sum of orbital energies

weighted by the orbital densities [54,61] and according to its interpretation, it is a better descriptor than MEP, when it comes to the identification molecular sites sensitive towards the electrophilic attacks. MEP and ALIE surfaces of PIDAA have been presented in Fig. 3. MEP and ALIE surfaces identify two different regions as possibly sensitive towards the electrophilic attacks. MEP surface recognizes oxygen atoms (double bonded to carbon atoms) as molecular sites with the lowest MEP values, and therefore as sensitive towards the electrophilic attacks. On the other side, ALIE surface recognizes nitrogen atom and benzene ring carbon atoms as molecular sites where the electrons are least tightly bonded, indicating the sensitivity of these locations to electrophilic attacks as well. MEP surface indicates that the hydrogen atoms of the OH groups are characterized by the highest MEP and therefore should be sensitive towards the nucleophilic attacks. These molecule sites are also characterized by the highest ALIE values.

3.6. Hyperpolarizability analysis

A large degree of hyperpolarizability is a useful measure to determine potential materials for optoelectronic applications. The relationship between the structure of the molecule and the optical properties helps in designing materials for such applications [62] which can be

Table 4
Dipole moment, static polarizability and first hyperpolarizability components of PIDAA by B3LYP/6-311++G(d,p).

Property	Parameter	PIDAA			Urea
		B3LYP/6-311++G(d,p)	B3LYP/cc-pvtz	B3LYP/aug-cc-pVDZ	B3LYP/6-311++G(d,p)
Dipole moment, μ(debye)	μ_x	−0.267	−0.216	−0.270	−0.806
	μ_y	−0.109	−0.142	−0.107	1.543
	μ_z	1.034	1.024	1.051	−0.008
	μ(D)	1.073	1.057	1.091	−1.741
Polarizability, α(esu)	α_{xx}	181.035	177.225	187.347	37.245
	α_{xy}	−5.063	−5.044	−5.304	−0.194
	α_{yy}	126.505	121.855	130.418	37.988
	α_{xz}	−0.338	1.237	0.728	0.052
	α_{yz}	−4.535	−5.046	−4.789	−0.063
	α_{zz}	117.193	107.532	122.219	24.012
	α (a.u)	141.578	135.537	146.662	33.081
	α (e.s.u)	2.098×10^{-23}	2.009×10^{-23}	2.174×10^{-23}	0.491×10^{-23}
	$\Delta\alpha$ (a.u)	39.2	313.513	330.260	65.933
	$\Delta\alpha$ (e.s.u)	4.731×10^{-23}	4.646×10^{-23}	4.895×10^{-23}	0.9771×10^{-23}
First hyperpolarizability, β(esu)	β_{xxx}	−302.594	−267.131	−324.230	23.748
	β_{xxy}	−13.708	−25.128	−17.213	17.376
	β_{xyy}	−19.404	−22.997	−23.741	−55.468
	β_{yyy}	31.614	38.977	32.102	44.220
	β_{zxx}	66.141	79.580	76.405	−0.489
	β_{xyz}	−30.979	−42.606	−33.508	0.034
	β_{zyy}	10.975	26.969	12.425	−0.531
	β_{xzz}	−36.780	33.738	−21.162	−19.037
	β_{yzz}	−4.397	12.557	−11.405	33.038
	β_{zzz}	−20.470	−20.851	−20.470	−1.062
	β_o (a.u)	363.473	271.620	375.425	107.407
	β_o (e.s.u)	3.140×10^{-30}	2.347×10^{-30}	3.243×10^{-30}	0.927×10^{-30}

Table 5
Comparison of the electronic properties of PIDAA attained experimentally (DMSO and distilled water) and calculated by TD-DFT/B3LYP method.

Experimental				Excited state	TD-B3LYP/6-311++G(d,p)										
DMSO		Distilled water			Gas phase				Solvent phase (DMSO)				Solvent phase (distilled water)		
λ_{max} (nm)	Band gap (eV)	λ_{max} (nm)	Band gap (eV)		λ_{cal} (nm)	Band gap (eV)	Energy (cm^{-1})	f*	λ_{cal} (nm)	Band gap (eV)	Energy (cm^{-1})	f*	λ_{cal} (nm)	Band gap (eV)	Energy (cm^{-1})	f*
321	3.865	316	3.964	S$_1$	321	3.87	31,194	0.02	313	3.965	31,958	0.02	313	3.967	31,975	0.02
319	3.889	311	3.989	S$_2$	298	4.16	33,532	0.03	306	4.054	32,678	0.05	306	4.055	32,679	0.05
316	3.926	308	4.028	S$_3$	293	4.23	34,096	0.06	294	4.213	33,957	0.03	294	4.214	33,968	0.03

established using DFT. B3LYP/6-311G(d,p), B3LYP/aug-cc-pVDZ (Dunning) and B3LYP/cc-pvtz methods were employed to determine the microscopic optical properties of PIDAA. Computations using Dunning's correlation consistent basis set have a benefit that it has additional functional implemented in the basis set i.e. augmented with additional polarization and diffuse functions and hence higher precision is attained from the calculated values from this functional when compared to the values calculated from other two combinations.

The highest values of the dipole moment were found to be 1.034D along μ_z computed from B3LYP at 6-311++G (d,p) basis set. For the X and Y directions, the values are equal to −0.267 and −0.109D, as shown in Table 4. Sufficiently high value of dipole moment which was almost similar to the dipole moment of urea (1.741D) shows strong intermolecular interactions. The polarizability component, α_{xx} has a greater influence on the static polarizabilities. α and β varied depending on the type of DFT methods. Urea is frequently used as a threshold value for comparative studies since it is a prototypical molecule used in the study of the nonlinear optical (NLO) properties of molecular systems [63]. The first order hyperpolarisability total value for the title molecule calculated is 3.140×10^{-30} esu which is about 3.5 times greater than that of urea (0.92793×10^{-30} esu). This large hyperpolarisability value of the title molecule indicates that it has considerable NLO properties. The π-electron cloud movement from donor to acceptor might be responsible for the molecule to be highly polarized and thus makes the intra- molecular charge transfer possible. PIDAA may be thus a potential applicant in the development of NLO materials.

3.7. Electronic spectral analysis

UV–visible analysis of PIDAA was carried out using TD-DFT method at B3LYP/6-311++G (d,p) level of basis set. The calculated absorption peak, excitation energies and oscillator strength (f) were presented in Table 5. Due to the specific solute-solute and solute-solvent interaction in form of hydrogen bonding, the intensities, positions and shapes of the electronic absorption bands are usually altered when the absorption spectra are recorded in solvents of different polarity.

Electronic spectrum of PIDAA in DMSO solvent reveals the absorption peaks at 316, 319 and 321 nm due to π → π* and n → π* transition and the small peak attained at 229 nm is accredited to the solvent DMSO as seen in Fig. 4. The absorption spectra of PIDAA in DMSO solution are slightly red shifted when compared to the spectrum in distilled water (308, 311 and 313 nm), indicating relatively strong guest–host interaction between the title molecule and the DMSO environment resulting in spectral shifts. The dipolarity/polarizability, π* = 1, the scale of the solvent hydrogen bond acceptor (HBA) basicities = 0.76 and scale of the solvent hydrogen bond donor (HBD) acidities, α = 0 for DMSO solvent. In addition to the wavelength of absorbance of DMSO to be coinciding with the title molecule's UV range, the presence of sulphur with a double bonded oxygen brings alteration in the spectra. The solvent polarity and dipole increased, resulting in the polarity of the solute to increase. It also caused the maximum wavelength red shift and decreased the absorbance as observed at 321 nm. The result showed that π bonding orbital structure jumped into antibonding π* orbital. The band gap obtained in the presence of DMSO and distilled water ranged between 3.865–3.928 eV and 3.964–4.028 eV respectively. When compared to

the theoretically obtained energy gap from the FMO analysis this value showed slight deviations due to the difference in phase of measurement.

In the solid state, the π → π* absorption is at 293.292 nm and n → π* transition is red shifted to 320.577 nm. It is noted theoretically that PIDAA has no absorption in the entire visible region and low energy band gap which is an essential feature for the frequency doubling process in solid state lasers [64]. The calculated band at 320.577 nm in the theoretical spectrum corresponds to the transition of HOMO to LUMO (97%). The second dominant band observed at 298.223 nm in the theoretical spectrum corresponds to the transition of HOMO to LUMO+1 (90%). The third dominant band observed at 293.292 nm for PIDAA originates mainly from the transitions between HOMO to LUMO +2 (63%) and by the minor contributions from HOMO to LUMO+3 (25%) and HOMO to LUMO+5 (2%).

3.8. Frontier molecular orbital analysis

The HOMO-LUMO energies and the energy gap between them calculated at B3LYP/6-311 G(d,p) level are −5.677, −0.926 and 4.751 eV respectively. The low energy gap associated with PIDAA denotes a reactive nature in this molecule. The comparatively low value of band gap has its application in modifying the properties of optical devices. The distributions and energy levels of the HOMO−2, HOMO−1, HOMO, LUMO, LUMO +1 and LUMO+2 orbitals computed at the B3LYP/6-311+G(d,p) level for the title compound are represented in Fig. 5. HOMO is slightly delocalized in carbon atoms with greater influence on the rest of the groups while LUMO is mainly delocalized in carbon atoms of the phenyl ring. HOMO−1 is delocalized over the carbon atoms of phenyl ring with lesser influence and LUMO+1 is localized on the phenyl ring as well as over the nitrogen atom. HOMO−2 is delocalized over the carbonyl group and LUMO+2 is localized on the phenyl ring and the nitrogen atom
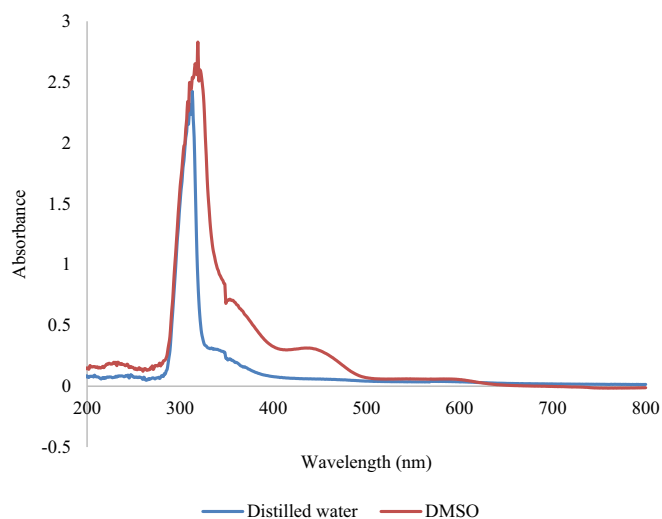

Fig. 4. Experimental UV–Vis absorption spectra of PIDAA in solvents DMSO and distilled water.
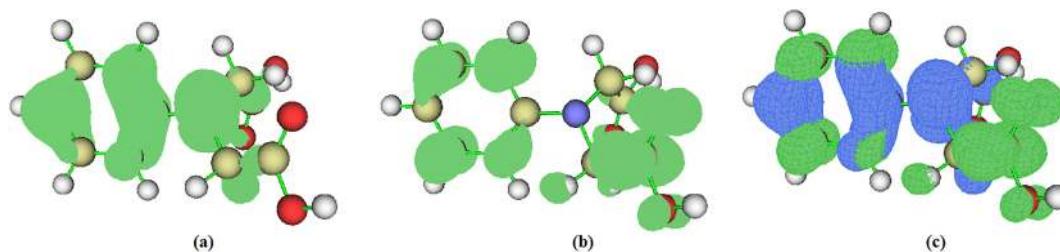
Fig. 5. Atomic orbital HOMO - LUMO composition of the frontier molecular orbital of PIDAA.

with slight influence over the carbonyl group. Due to the strong electron-acceptor ability of the electron-acceptor group, the LUMO has higher stability leading to low HOMO–LUMO band gap. The calculated energy values are presented in Table 6 which reveals the chemical reactivity of title compound and proves the occurrence of eventual charge transfer within the molecule. The molecule is not very hard owing to the chemical hardness (2.375) with strong energy transformation [65]. The toxicity of the title molecule is substantially low due to low softness value (0.210). Electrophilicity index is one of the crucial Conceptual Density Functional Theory (CDFT) based descriptor used to study bio-activities [66]. The sufficiently high value of the electrophilicity index (2.294) acts as a precursor to analyzing the title molecule for its biological activity in terms of molecular docking where the title compound PIDAA is the ligand and is docked to a suitable protein.

The TDOS, PDOS and the COOP spectra were plotted as seen in Fig. S2. A realistic description of the FMOs cannot be achieved considering only the HOMO and LUMO. Thus, TDOS, PDOS and COOP were calculated and created by convoluting the MO information with Gaussian curves. The fragment orbitals contributing to the MO were majorly by the C—O orbitals followed by the O—H, N—C and least by the C—H.

Table 6
Calculated energy values of the PIDAA by B3LYP/6-311++G (d, p).

Molecular properties	Energy (eV)	Energy gap (eV)	Ionization potential (I)	Electron affinity (A)	Global hardness (η)	Electro negativity (χ)	Global softness (σ)	Chemical potential (μ)	Global electrophilicity (ω)
E_{HOMO}	−5.6766	4.751	5.677	0.926	2.375	3.301	0.210	−3.301	2.294
E_{LOMO}	−0.926								
E_{HOMO-1}	−6.9879	6.319	6.988	0.669	3.160	3.828	0.158	−3.828	2.319
E_{LUMO+1}	−0.6686								
E_{HUMO-2}	−7.0864	6.457	7.086	0.630	3.228	3.858	0.155	−3.858	2.305
E_{LUMO+2}	−0.6297								

Fig. 6. Visualization of the (a) hole distribution (b) electron distribution (c) the hole and electron distributions (represented as blue and green isosurfaces respectively).

The overlap on C—H with O—H (very weak) and N—C with C—O (medium) is due to the positive overlap population (bonding interactions) while the overlap on N—C with O—H (very weak), C—H with C—O (strong) and C—H with N—C (very strong) is due to the negative overlap population (anti-bonding interactions).

A correlation is drawn been the trends associated with the HOMO-LUMO gap with charge transfer that occurs as a consequence of the first three excitations. The Multiwfn [67–69] program has been employed to reconnoiter the charge transfer (CT) due to the first excitation by examining electron density variation [70]. In addition, the calculation of Δr index [71] is a quantitative indicator of electron excitation mode. The initial calculations show that the excitation mode 1, 2 and 3 possess a strong probability to exhibit Charge Transfer excitation or Rydberg character since the values of Δr are >2.0 Å. However final conclusions can be made only after the visualization of the electron and hole distribution. On visualization, it was observed that the result generated by the medium quality grid for the integral of the hole (0.9700), electron (0.9697) and transition density ($\approx$0) lie in concurrence with the ideal values. The distance between the centroid of hole and electron is a measure of CT length. The considerably small value indicates the shorter length for the charge transfers. The RMSD of hole distribution that provides an insight into the distribution breadth shows it is much broader in X direction in comparison to the Y and Z direction. The t

index that measures the extent of separation between the hole and electron in the title compound shows negative values along the X, Y and Z direction. The distribution of hole, electron and both simultaneously are shown in Fig. 6 (at default isovalue 0.002). It can be observed that there is a spatial separation between the hole-electron distribution thus indicating charge transfer. From the output, we can see that the integral of overlap of hole-electron distribution (S) is 0.2907 for transition mode 1 which is greater when compared to transition mode 3 (0.1288). The distance between the centroid of hole and electron (D) for mode 3 (2.3487 Å) which is larger when compared to that of mode 1 (0.9981 Å). These quantitative data show that transition mode 3 has conspicuously stronger CT character than mode 1.

3.9. Vibrational spectral analysis

Based on FT-IR, FT-Raman spectra and vibrational wavenumbers computed at B3LYP/6-311++G (d,p) level of basis set the vibrational spectral analysis is carried out. Both the theoretical and experimental FT-IR and FT-Raman spectra are depicted in Figs. 7 and 8 respectively with a Pure Lorentzian band shape. The computed and experimental wavenumbers and their assignments are presented in Table 7. The title molecule has 26 atoms leading to 72 fundamental vibrations which show C_S and C_1 point group symmetry with all the vibrations
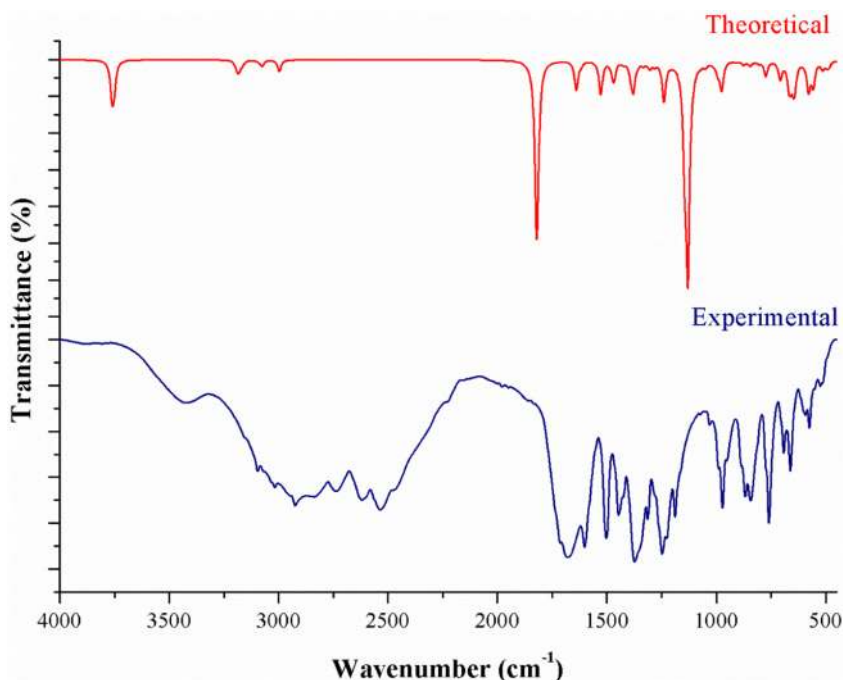

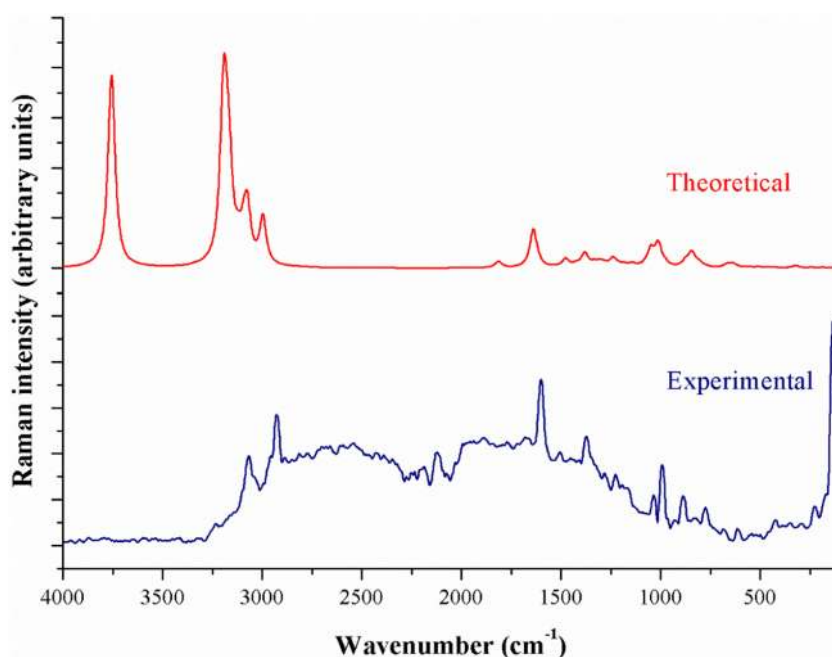**Fig. 7.** FT-IR spectra PIDAA using DFT/6-311++G (d,p) and experimental data

Fig. 8. FT-Raman spectra of PIDAA using DFT/6-311++G (d,p) and experimental data

active in both FT-IR and FT-Raman. The significantly high percentage of Potential Energy Distribution attained for most of the fundamental modes of vibration shows the greater stability of the molecule under C_1 symmetry with 27 stretching, 43 bending and 16 torsion coordinates.

The hydroxyl group stretching vibrations generally appear in the region around 3500 cm^{-1} [72,73]. In the IR spectrum, a broad intense band observed at 3423 cm^{-1}, is assigned to OH stretching vibration, and its intensity is less than that of free OH vibration due to the existence of intermolecular hydrogen bonding. Theoretically, the stretching vibrations are observed at 3611(O15-H26) and 3603 (O11-H23) cm^{-1}. The in-plane OH deformations appear in the region 1440–1260 cm^{-1} [74]. A medium band at 1313 and a strong band at 1073 cm^{-1} in IR is assigned to the in-plane bending vibration of OH group. This pure mode shows 100% PED contribution. In general, the aromatic CH stretching bands commonly exhibit multiple peaks in the spectral range of 3100–3000 cm^{-1} [75] with strong Raman intensity. There is a possibility for the absence of Raman bands in certain expected regions in the experimental spectra due to high levels of polarization in this domain. The title compound has five C—H moieties of the benzene ring in addition to two isolated CH bonds. The expected C—H stretching vibrations correspond to mode numbers from 62 to 70. The calculated frequencies of the C—H stretching vibrations 3070, 3062, 3054, 3042, 3035, 2996, 2969, 2952 and 2880 cm^{-1} show very good agreement with experimental data 3095, 3017, 2924 and 2837 cm^{-1} in the IR spectrum as weak bands. The PED of these C—H stretching vibrations is almost pure.

A varying level of strong and weak intensity bands are observed in case of CH in-plane ring bending vibrations in the region 1300–1000 cm^{-1} [76]. CH in-plane bending vibrations of the present compound is found at 1469 and 1136 cm^{-1} theoretically and experimentally between 1446 and 1189 cm^{-1} of the FT-IR spectrum while between 1507 and 1227 cm^{-1} of the FT-Raman spectrum. The interference of the in and out-of-plane bending vibrations of other functional groups such as CC and CN with low PED percentages leads to the slight overestimation in this region. The C=O stretching vibrations have a strong absorption band which is expected in the region of 1850–1550 cm^{-1} [77]. The frequency of the stretching vibration is decreased due to the localization of p electron conjugation thus leading to a decrease in the double bond character of the C=O group. In the

molecule, a comparatively medium strength band in FT-Raman spectrum at 1886 and 1680 cm^{-1} was assigned to C=O stretching vibration. Theoretically, vibrations are observed at 1750 and 1741 cm^{-1} with significant PED contribution. The medium peak observed in the Raman spectrum is due to p electron releasing effect in the C=O that causes a change in the polarizability during vibrational motion.

The compound containing C—O group causes absorption as a very strong band at 1310–1095 cm^{-1} [78]. The recorded spectrum shows sufficiently strong band in FT-IR spectrum at 1073 cm^{-1} and theoretically at 1100 and 1086 cm^{-1} which are in good agreement with each other. The computed CO in-plane bending vibrations attained in the lower frequency region range. The bands in the range of 1650–1400 cm^{-1} are assigned to carbon vibrations [79] while the ring stretching vibrations (C=C) is expected within the region 1300–1000 cm^{-1} [80]. In the present study the FT-IR bands observed at 1601, 1502, 1030 and 843 cm^{-1} and Raman bands observed at 1600 and 1035 cm^{-1}. The theoretical frequencies assigned to CC stretching vibrations are 1576, 1555, 1427, 1306, 1064, 1032, 935, 840 and 812 cm^{-1}. The PED of these vibrations for both the molecules is mixed modes. The skeletal CC vibrations are not disturbed by the substitutional groups. However, the addition of substituents brings considerable variations in the C=C stretching which is attributed to the fact that an interference is caused by CN bands which also coincides with this range. The C–C–C trigonal bending modes are assigned to the bands at 1555, 973, 744 and 616 cm^{-1}. As it is evident from PED the C-C-C trigonal bending mode is a mixed mode.

Frequency nearer to 1500 cm^{-1} indicates C=N bonds while frequency nearer 1300 cm^{-1} indicates the presence of C—N bonds [81]. The band at 1247 and 1226 cm^{-1} in FT-IR and 1227 cm^{-1} in FT-Raman is assigned to C—N stretching vibration indicates the presence of C—N bond. The theoretically scaled values at 1191 and 1176 cm^{-1} correlate with experimental observation. The PED of these vibrations is mixed modes.

3.10. Chemical bonding analysis

The impetus for a density-based description of chemical bonding led to the development of new descriptors such as the electron localization function (ELF) introduced by Becke and Edgecombe [82] and localized-

Table 7
Observed and calculated vibrational frequency of PIDAA at B3LYP method with 6-311++G (d,p) basis set.

| Experimental		Theoretical		IR		Raman		Assignments (PED)[d]
Frequency (cm^{-1})		Frequencies (cm^{-1})		Intensity		Intensity		
FT-IR	FT-Raman	Unscaled	Scaled[a]	Absolute[b]	Relative	Absolute[c]	Relative	
3625(w)	–	3762	3611	86	16	186	85	γ OH (100)
–	–	3753	3603	67	12	218	100	γ OH (100)
–	–	3198	3070	3	1	180	83	γ CH (89)
3095(m)	3067(m)	3190	3062	19	3	158	73	γ CH (98)
–	–	3181	3054	22	4	46	21	γ CH (82)
–	–	3169	3042	7	1	120	55	γ CH (93)
3017(m)	–	3162	3035	5	1	36	16	γ CH (98)
–	–	3121	2996	1	0	30	14	γ CH (99) + γ CH (84)
–	–	3093	2969	4	1	44	20	γ CH (96)
2924(s)	2928(m)	3075	2952	17	3	99	46	γ CH (100)
2837(m)	–	2997	2880	32	6	93	43	γ CH (97)
–	1886(m)	1821	1750	474	86	3	1	γ OC (85)
1681(vs)	1680(m)	1811	1741	30	5	10	5	γ OC (86)
1601(vs)	1600(s)	1640	1576	79	14	73	34	γ CC (51)
1502(vs)		1618	1555	9	2	9	4	γ CC (50) + β CCC (−10)
1446(s)	1507(m)	1528	1469	91	17	1	1	β HCC (69)
–	–	1484	1427	2	0	2	1	γ CC (20) + β HCC (34)
–	–	1476	1418	11	2	13	6	τ HCCO (25) + β HCH (28)
–	–	1468	1411	50	9	2	1	β HCH (73) + τ HCCO (10)
1373(vs)	1374(m)	1424	1369	6	1	5	2	β HCH (34) + τ HCCO (21)
–	–	1391	1337	31	6	3	2	τ HCCO (29) + β HCH (16)
–	–	1379	1326	74	13	24	11	β HCC (62)
–	–	1359	1306	7	1	1	1	γ CC (52)
1313(s)	–	1333	1281	10	2	7	3	β HOC (17) + β HCC (12) + τ HCCO (20)
–	–	1308	1257	7	1	4	2	β HOC (44)
–	–	1302	1251	12	2	6	3	β HOC (27) + β HCC (39)
–	–	1281	1231	10	2	5	2	β HCC (31)
1247(s)	–	1239	1191	106	19	16	7	γ NC (29) + β HCC (15)
1226(vs)	1227(w)	1224	1176	1	0	2	1	γ NC (29) + β HCC (17)
–	–	1207	1160	4	1	3	1	β HCC (75)
1189(s)	–	1182	1136	1	0	4	2	β HCC (72)
–	–	1145	1100	200	36	5	2	γ OC (51) + β HOC (28)
1073(w)	–	1130	1086	553	100	1	1	γ OC (54) + β HOC (24)
–	–	1107	1064	5	1	0	0	γ CC (46) + β HCC (15)
1030(w)	1035(w)	1074	1032	5	1	3	2	γ CC (39)
–	–	1049	1008	12	2	33	15	τ HCCO (27)
990(m)	992(w)	1012	973	4	1	45	21	β CCC (73)
972(m)	–	994	955	24	4	1	0	τ HCCO (35) + ω OCOC (28)
952(m)	–	990	952	1	0	0	0	τ HCCN (35) + τ CCCC (24)
–	–	977	939	66	12	5	3	τ HCCN (90)
–	–	973	935	12	2	0	0	γ NC (51) + γ CC (12)
867(s)	887(w)	906	871	3	1	0	0	τ HCCN (46) + τ CCCC (13) + τ HCCN (27)
843(s)	–	875	840	12	2	10	5	γ CC (41) + β CCN (11)
–	–	845	812	12	2	24	11	γ CC (51) + β CCN (12)
–	–	835	802	2	0	6	3	τ HCCN (95)
759(s)	775(w)	806	775	7	1	8	4	τ HCCN (65) + ω NCCC (14)
–	–	774	744	41	7	2	1	γ NC (14) + β CCC (66)
692(m)	–	708	680	48	9	0	0	τ CCCC (35) + ω NCCC (14) + τ HCCN (29)
662(m)	–	668	642	55	10	4	2	γ OC (12) + β HCH (29) + β CCN (13)
–	–	660	635	33	6	2	1	τ HOCC + ω OCOC (30)
–	–	647	622	44	8	0	0	τ HOCC (42) + ω OCOC (24)
–	615(w)	641	616	47	9	4	2	β HCH (26) + β CCC (32)
592(w)	–	631	607	1	0	4	2	β CCC (25) + β HCH (34)
574(w)	–	579	556	78	14	1	1	β HCH (17) + β NCC (12) + ω NCCC (12)
–	–	557	535	65	12	2	1	τ HOCC (75)
525(w)	–	513	493	22	4	2	1	τ HOCC (43) + ω OCOC (24)
–	–	493	474	10	2	0	0	β OCC (29) + ω NCCC (23)
–	–	485	466	14	2	1	0	β NCC (24) + ω CCCN (11)
–	422(w)	442	424	4	1	2	1	τ HCCN (25) + τ CCCC (64)
–	–	418	402	1	0	1	0	γ NC (14) + β OCC (34)
–	–	346	333	2	0	1	0	β CCC (12) + β OCC (18) + β NCC (10)
–	–	321	309	0	0	5	2	β OCC (26) + β NCC (15)
–	–	303	291	1	0	0	0	β NCC (20) + β CCN (20)
–	226(w)	243	233	2	0	1	1	β CCN (45)
–	–	196	188	4	1	1	0	τ CCCC (13) + τ CCNC (35)
–	135(vs)	174	167	6	1	1	0	τ CCNC (48)
–	95(s)	120	115	3	1	1	0	β CCN (14) + τ CCNC (17) + ω CCCN (16) + β NCC (14)
–	–	55	53	1	0	1	0	τ OCCN (31) + ω CCCN (−29)
–	–	51	49	1	0	4	2	β NCC (12) + τ OCCN (56) + τ CNCC (11)
–	–	45	44	1	0	1	0	τ OCCN (38) + τ CCNC (37)
–	–	38	37	0	0	5	2	τ CNCC (72)
–	–	36	35	1	0	3	1	γ NC (10) + β NCC (31) + τ CCNC (12)
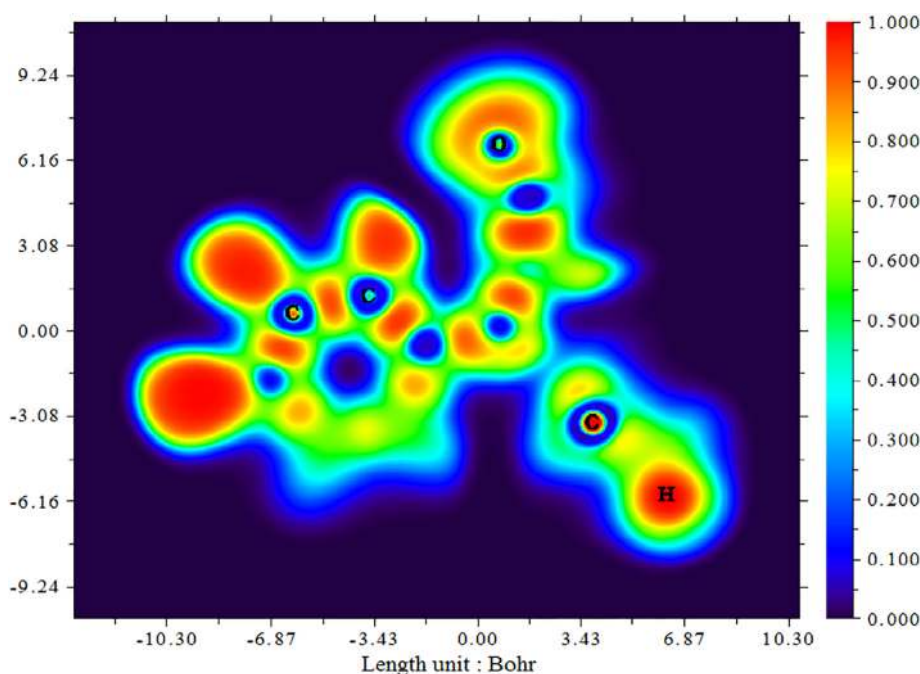
Fig. 9. Color-filled map of electron localization function of PIDAA.

orbital locator (LOL) [83,84], These methods are mainly based on topological methods. The kinetic-energy density, τ acts as the central property on which the localization descriptors are built on since the lowering of the quantum kinetic-energy density by orbital sharing is the driving force of covalent bonding [85,86]. Consideration of the electron pair density is the foundation of ELF while LOL simply recognizes that gradients of localized orbitals are maximized when localized orbitals overlap.

3.10.1. Electron localization function (ELF)

Electron delocalization is an important parameter to explain the aromaticity of a molecule, the nature of chemical bonding in transition metal complexes [87] and most importantly it directly reveals the Pauli exchange repulsion effect by measuring the excess of local kinetic energy due to Pauli repulsion which has several applications in VSEPR theory [88]. It was observed that high value occurs between the carbon atoms in the phenyl ring while the values are higher between the boundary carbon atoms in the ring with the hydrogen atom. This is because of the overlap of the sp. orbital of carbon with the s orbital of the hydrogen which is electronically more stable. By examining the value of the carbon and nitrogen atom (C2-N1) the bonding is considerably weaker with the lowest value between N1-C9. This observation can be substantiated from the NBO output where the stabilization energy between the nitrogen and carbon atoms is low. Furthermore, an n-σ* anomeric effect is expected between the lone pair on the carbonyl oxygen atom [89]. This leads to a deformation of the ELF distribution around the oxygen atom of the carbonyl group as observed in Fig. 9. By examining ELF values of oxygen along the carboxylic acid group, values were lower (represented by blue). The electrons in the bonds between the carbon carbon atoms showed localization (represented by red region) in comparison to the electrons in the bonds between carbon hydrogen (represented by green region).

3.10.2. Localized orbital locator (LOL)

Molecular orbitals which are concentrated in a limited spatial region constitute the Localized molecular orbitals. Fig. 10 shows its Localized Orbital Locator (LOL) distribution under 6-311++G(d,p) basis set. It is worth noting that the red color in Fig. 10 somewhat intrudes into the interstitial space between boundary atoms. The low stabilization energy as observed from the NBO results between the carbon nitrogen bonds is reflected as comparatively low values in the LOL figure and a distortion between the N1-C9 atoms [83,84,90].

3.11. Sensitivity towards autoxidation and influence of water

Sensitivity towards the autoxidation mechanism can be predicted by the DFT calculations since the correlation between this mechanism and bond dissociation energy for hydrogen abstraction (H-BDE) has been established [91]. This is of great practical importance, since oxidative reactions are very significant for the removal of organic pollutants through their degradation [92]. Sensitivity towards the autoxidation mechanism is indicated if the calculated H-BDE values are between 70 and 85 kcal/mol [93,94], while the region between 85 kcal/mol and 90 kcal/mol could also be of importance for autoxidation, but must be taken with caution [94]. According to the results of H-BDE provided in Fig. 11, PIDAA might have interesting sensitivity towards the autoxidation mechanism.

Calculated H-BDE values indicate that the large part of the PIDAA molecule might be sensitive towards the autoxidation mechanism. Namely, hydrogen atoms of carbon atoms C9 and C13 might be highly sensitive towards the autoxidation mechanism since the calculated H-BDE values are having values of ~80 kcal/mol. Hydrogen atoms belonging to OH group might also be sensitive towards the autoxidation, with the calculated H-BDE values of ~83 kcal/mol. Understanding stability of pharmaceutical molecules in water is of high importance not only for

Notes to Table 1:
[a]　Scaling factor: 0.96 above 3000 cm^{-1} and 0.961 below 3000 cm^{-1} for B3LYP/6-311+G(d,p)
[b]　Relative absorption intensities normalized with highest peak absorption equal to 100.
[c]　Relative Raman intensities normalized to 100.
[d]　γ-Stretching, β- bending, ω – out of plane, τ-torsion, vs-very strong, s- strong, m-medium, w-weak.
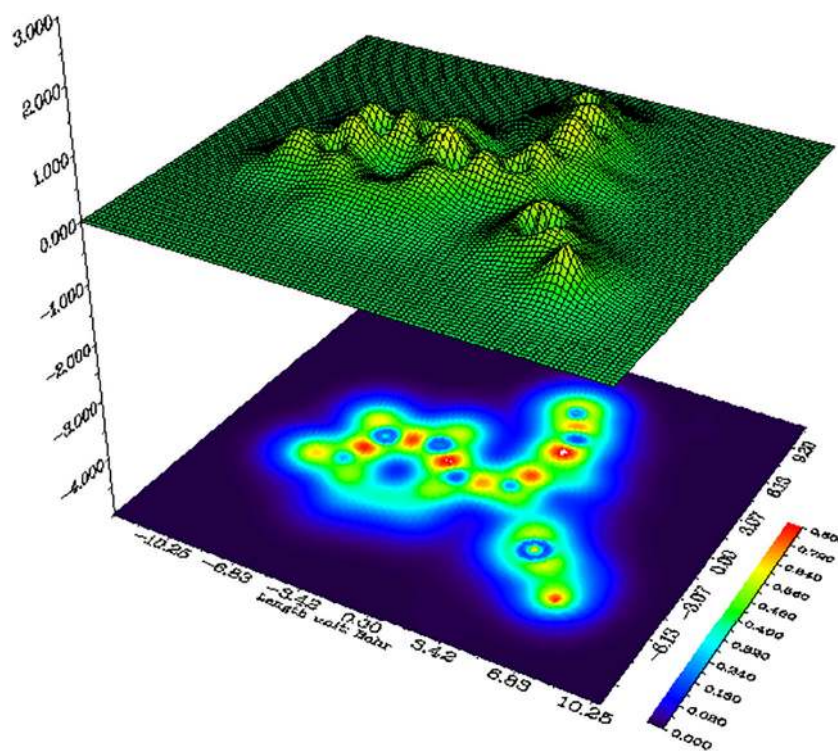
Fig. 10. Relief map with projection of localized orbital locator of PIDAA.

predicting their pharmacokinetics, but also to be able to understand the influence of hydrolysis mechanism with respect to degradation procedure. For these purposes, we have performed MD simulations and calculated radial distribution functions (RDF), in order to identify atoms with pronounced interactions with water molecules. For PIDAA, RDFs for atoms with significant interactions with water molecules are visualized in Fig. 12.

3.12. Solubility parameter

Excipients are substances that improve several pharmaceutical properties of a compound including stabilization, solubility, loading, etc. Frequently used excipients are polymer polyvinylpyrrolidone (PVP) or sugar molecules such as maltose or sorbitol. The degree of compatibility between drug candidate and potential excipient is replicated through similar values of the solubility parameter.

Employing MD simulations, solubility parameters of PIDAA molecule were calculate and compared with solubility parameters of frequently used excipients such as PVP, maltose and sorbitol. Solubility parameters of title molecule as well as excipient substances have been summarized in Table 8.

Solubility parameter δ of title molecule has the closest value to solubility parameter of maltose indicating that this molecule might be efficient excipient in case of the title molecule. A higher difference of 4.117 MPa$^{1/2}$ is observed between the solubility parameters of PIDAA and sorbitol. Difference between title molecule and PVP solubility parameters has a maximum value of 9.793 MPa$^{1/2}$. The compatibility of
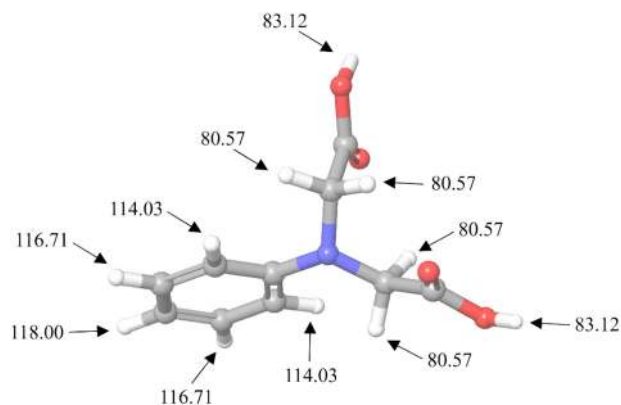
Fig. 11. H-BDE values of PIDAA.
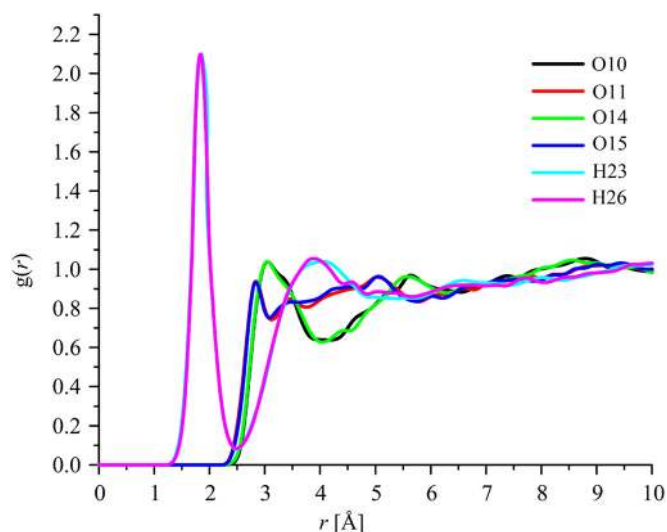
Fig. 12. Representative RDFs of PIDAA's atoms.

Table 8
Solubility parameters of PIDAA and frequently used excipient substances.

Compounds	δ (MPa$^{1/2}$)	Δδ (MPa$^{1/2}$)
N-Phenyliminodiacetic acid	28.308	–
PVP	18.515	9.793
Maltose	28.564	0.256
Sorbitol	32.425	4.117

Table 9
Drug likeness parameters of PIDAA.

Descriptor	Values
Hydrogen bond donor (HBD)	0
Hydrogen bond acceptor (HBA)	0
AlogP	0.904
Polar surface area (PSA) [Å^2]	77.840
Molar refractivity	52.656
Number of atoms	26
Number of rotatable bonds	5

the excipient with the title compound has the following order: Maltose > sorbitol > PVP. This implies that using maltose as the excipient can improve the bioactivity of the drug.

3.13. Drug likeness

Calculated values of the drug likeness parameters have been provided in Table 9. For the initial classification of drug candidates, it is important to consider the famous Lipinski's rule of five [95,96]. The parameter indicating lipophilicity/hydrophobicity, the AlogP, in case of the PIDAA is equal to 0.904, which is much lower than the values defined by Congreeve et al. [97], according to which logP values should be lower than 3. AlogP value of PIDAA indicates that this molecule might be considered as a lead drug candidate. HBD and HBA should be

<5 and 10, respectively, and these conditions are also fulfilled in case of PIDAA. The number of rotatable bonds is also within the desired range. PSA should be lower than 140 Å^2, while molar refractivity according to Ghose et al. [98] should take values in the range between 40 and 130. Conditions for both PSA and molar refractivity are satisfied, further emphasizing the pharmaceutical potential of PIDAA.

The biological activities of a group of SARSs drugs that are commercially available such as Lopinavir, Oseltamivir and Ribavirin [1–5] along with the title molecule PIDAA are related to various physiochemical parameters as seen in Table S3 in order to analyze if the later possess traits to be considered as a good SARS drug candidate. The low softness value of the title molecule, with value almost equal to that of Oseltamivir suggests the non-toxic nature while the comparable electrophilicity index with the other drugs (greater than Oseltamivir and Lopinavir) shows the biological activity. The comparison drawn between the physiochemical parameters of the drugs with the title compound provides further evidence that the title molecule is a potential SARS drug.

3.14. Molecular docking studies

Docking aids in the explication of the most energetically favorable binding pose of a ligand to its receptor in terms of the binding energy. The objective of our current docking study is to elucidate the mode of interaction of the ligand PIDAA with the protein 4APH, an Angiotensin converting enzyme, thus studying its prospective as a SARS drug. Target protein, 4APH was retrieved from the Protein Data Bank. All bound waters and cofactors were removed from the protein manually, Geisteger and Kollman charges were computed, polar hydrogen atoms were added subsequently and the AutoDock atom types were defined using AUTODOCK.

The Ramachandran plot [99] which displays the phi-psi torsion angles for all residues in the structure is shown in Fig. 13. It can be observed that most of the amino acids (95.2%) were present in the darkest region depicted here as red while no residues where present
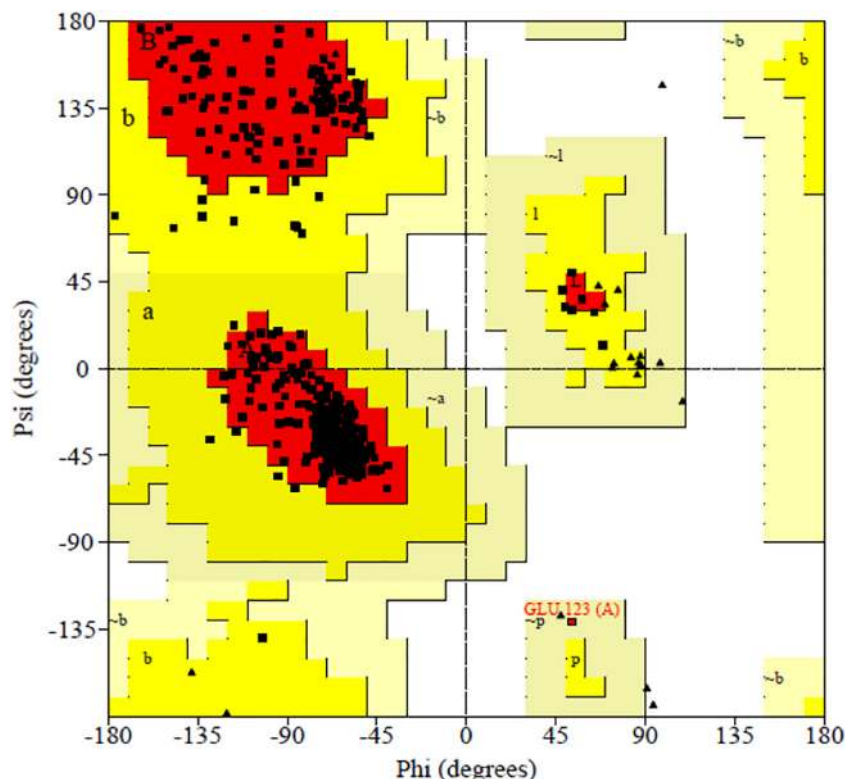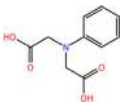

Fig. 13. Ramachandran plot of 4APH protein.

Table 10
Hydrogen bonding and molecular docking of PIDAA with 4APH protein target.

Ligand	Protein PDB ID	Binding amino acid residues	Binding energy (kcal/mol)	Inhibition constant (uM)	Ligand efficiency
	4APH	LYS'395/HZ2 with 13 atoms; GLY'362 with 4 atoms; LYS'363/HZ2 with 13 atoms; LYS'363/HZ3 with 13 atoms	−6.66	502.53	−0.3

in the disallowed regions. This ensures that the selected protein is highly stable in nature.

The Lamarckian Genetic Algorithm (LGA) was implemented in the AutoDock software for docking which has enhanced performance since it adds local minimization to the genetic algorithm and thus enabling modification of the gene population. On the basis of the binding energy, the docked conformations of the ligand were ranked into clusters and the top ranked conformations were visualized. The best conformation binding free energy was predicted to be −6.66 kcal/mol and the binding amino acid residues are shown in Table 10. The binding mode diagram is shown in Fig. 14 and this confirms the formation of interactions.

4. Conclusion

The optimization of structural geometry of PIDAA was done by B3LYP DFT functional which confirms the molecular geometry. Hyperconjugative interactions in NBO analysis support intramolecular nature of hydrogen bonding and charge transfer interactions where the electron donating from LP(2)O15 → π* (C12-O14) showed a maximum stabilization of 48.65 kJ/mol. The polar (θ) and azimuthal (φ) angles of the vector from the nucleus along with the deviation angle were used to specify the direction of a hybrid. The atomic charge calculations of the PIDAA showed O10 atom has the highest value of −0.269 e which is mainly due to the polar nature of the carbonyl group. Solid state UV spectroscopic analysis indicated π → π* and n → π* transitions of PIDAA with an energy gap of 4.536 eV in the third excited state. The chemical hardness (2.375) specified compound stability, low chemical softness (0.210) signified non-toxicity while the electrophilicity index (2.294) was a descriptor of biological activeness of PIDAA. The molecular structure of PIDAA was ascertained by using FT-IR and FT- Raman spectroscopic studies and vibrational assignments were analyzed. ELF studies showed the stronger chemical bonding between CH bonds due to the overlap of the sp. orbital of carbon with the s orbital of the hydrogen which is electronically more stable. MEP surface identifies oxygen atoms to be sensitive towards the electrophilic attacks, while ALIE
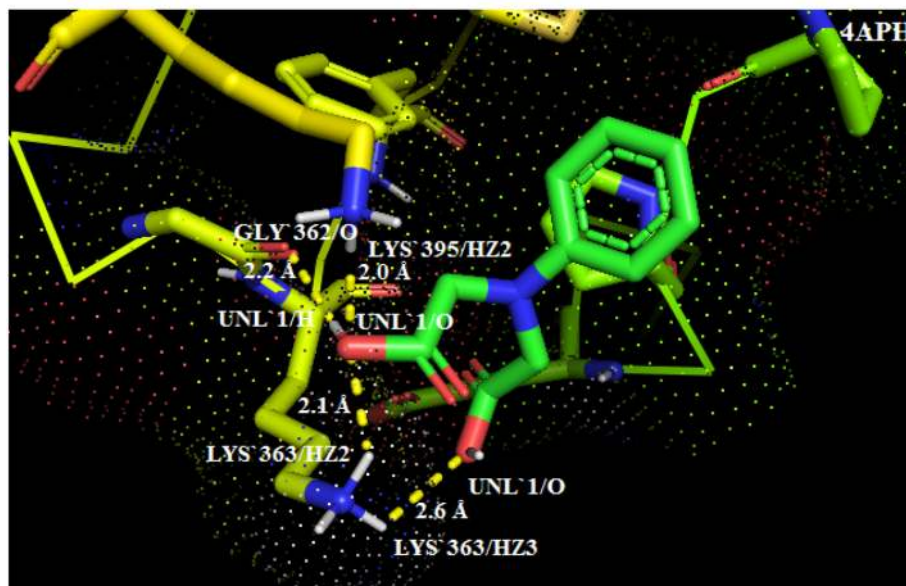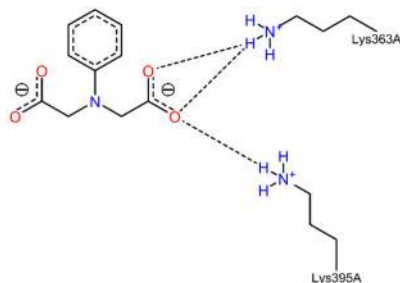

Fig. 14. PIDAA embedded in the active site of 4APH protein (2D and 3D representation).

surface identifies nitrogen atom and carbon atoms of the benzene ring to be sensitive towards the electrophilic attacks. DFT calculations indicate sensitivity towards the autoxidation mechanism, since H-BDE values of 6 hydrogen atom are having values lower than 85 kcal/mol. Maltose as the excipient can improve the bioactivity of the drug. The pharmaceutical potential of PIDAA is also indicated by the representative values of drug likeness parameters. The low stabilization energy as observed from the NBO results between the carbon nitrogen bonds was reflected as comparatively low values in the LOL figure and a distortion between the N1-C9 atoms. The biological activity of the molecule in terms of molecular docking has been analyzed theoretically for the treatment of SARS and minimum binding energy of −6.66 kcal/mol calculated.

Acknowledgment

Appendix A. Supplementary data

Supplementary data to this article can be found online at https://doi.org/10.1016/j.saa.2019.117188.

References

[1] W.C. Yu, D.S.C. Hui, M. Chan-Yeung, Antiviral agents and corticosteroids in the treatment of severe acute respiratory syndrome (SARS), Thorax 59 (2004) 643–645.
[2] E.L. Tan, E.E. Ooi, C.Y. Lin, H.C. Tan, A.E. Ling, B. Lim, L.W. Stanton, Inhibition of SARS coronavirus infection in vitro with clinically approved antiviral drugs, Emerg. Infect. Dis. 10 (4) (2004) 581–586.
[3] Hatem A. Elshabrawy, Jilao Fan, Christine S. Haddad, Kiira Ratia, Christopher C. Broder, Michael Caffrey, Bellur S. Prabhakar, Identification of a broad-spectrum antiviral small molecule against severe acute respiratory syndrome coronavirus and Ebola, Hendra, and Nipah viruses by using a novel high-throughput screening assay, J. Virol. 88 (8) (2014) 4353–4365.
[4] C.M. Chu, V.C.C. Cheng, I.F.N. Hung, et al., Role of lopinavir/ritonavir in the treatment of SARS: initial virological and clinical findings, Thorax 59 (2004) 252–256.
[5] B. Gopal Samy, Lawrence Xavier, Molecular docking studies on antiviral drugs for SARS, International Journal of Advanced Research in Computer Science and Software Engineering 5 (3) (2015) 75–79.
[6] Yan-Ping Ren, La-Sheng Long, Bing-Wei Mao, You-Zhu Yuan, Rong-Bin Huang, Lan-Sun Zheng, Nanoporous lanthanide–copper(II) coordination polymers: syntheses and crystal structures of [{M_2(Cu$_3$(iminodiacetate)$_6$)}·8H$_2$O]$_n$ (M=La, Nd, Eu), Angew. Chem. Int. Ed. 42 (5) (2003) 532–535.
[7] J.M. Antonucci, J.W. Stansbury, M. Farahani, Polymerization of dental resins via acid-amine interactions, J. Dent. Res. 71 (1992) 239.
[8] G.E. Schumacher, F.C. Eichmiller, J.M. Antonucci, Effects of surface-active resins on dentin/composite bonds, Dent. Mater. 8 (1992) 278–282.
[9] Hu Zhang-Jun, Jia-Xiang Yang, Hong-Wen Gao, Novel phenyl-iminodiacetic acid grafted multiwalled carbon nanotubes for solid phase extraction of iron, copper and lead ions from aqueous medium, Microchim. Acta 176 (2012) 359.
[10] J S M Peiris, Y Guan and K Y Yuen Nat. Med. 10 S88 (2004).
[11] Michael D. Christian, Susan M. Poutanen, Mona R. Loutfy, Matthew P. Muller, Clin. Infect. Dis. 38 (2004) 1420.
[12] G. Masuyer, S.L.U. Schwager, E.D. Sturrock, R.E. Isaac, K.R. Acharya, Molecular recognition and regulation of human angiotensin-I converting enzyme (ace) activity by natural inhibitory peptides, Sci. Rep. 2 (717) (2012).
[13] Bakhtiyor F. Rasulev, Nasrulla D. Abdullaev, Vladimir N. Syrov, Jerzy Leszczynski, A Quantitative Structure-Activity Relationship (QSAR) Study of the Antioxidant Activity of Flavonoids, 2005.
[14] G.L. de Souza, L.M. de Oliveira, R.G. Vicari, A. Brown, A DFT investigation on the structural and antioxidant properties of new isolated interglycosidic O-(1 → 3) linkage flavonols, J. Mol. Model. 22 (4) (2016) 1–9.
[15] Z. Sroka, B. Żbikowska, J. Hładyszowski, The antiradical activity of some selected flavones and flavonols. Experimental and quantum mechanical study, J. Mol. Model. 21 (2015) 12)1–11.
[16] H. Djeradi, A. Rahmouni, A. Cheriti, Antioxidant activity of flavonoids: a QSAR modeling using Fukui indices descriptors, J. Mol. Model. 20 (10) (2014) 1–9.
[17] S. Armaković, S.J. Armaković, S. Koziel, Optoelectronic properties of curved carbon systems, Carbon 111 (2017) 371–379.
[18] S. Armaković, S.J. Armaković, J.P. Šetrajčić, I.J. Šetrajčić, Active components of frequently used β-blockers from the aspect of computational study, J. Mol. Model. 18 (9) (2012) 4491–4501.
[19] S.J. Armaković, S. Armaković, N.L. Finčur, F. Šibul, D. Vione, J.P. Šetrajčić, B. Abramović, Influence of electron acceptors on the kinetics of metoprolol photocatalytic degradation in TiO 2 suspension. A combined experimental and theoretical study, RSC Adv. 5 (67) (2015) 54589–54604.
[20] M. Blessy, R.D. Patel, P.N. Prajapati, Y. Agrawal, Development of forced degradation and stability indicating studies of drugs—a review, Journal of Pharmaceutical Analysis 4 (3) (2014) 159–165.
[21] S. Armaković, S.J. Armaković, B.F. Abramović, Theoretical investigation of loratadine reactivity in order to understand its degradation properties: DFT and MD study, J. Mol. Model. 22 (10) (2016) 240.
[22] B. Sureshkumar, Y.S. Mary, C.Y. Panicker, S. Suma, S. Armaković, S.J. Armaković, C. Van Alsenoy, B. Narayana, Quinoline derivatives as possible lead compounds for anti-malarial drugs: spectroscopic, DFT and MD study, Arab. J. Chem. (2017).
[23] M.J. Frisch, G.W. Trucks, H.B. Schlegel, G.E. Scuseria, M.A. Robb, J.R. Cheeseman, J.A. Montgomery Jr., T. Vreven, K.N. Kudin, J.C. Burant, J.M. Millam, S.S. Iyengar, J. Tomasi, V. Barone, B. Mennucci, M. Cossi, G. Scalmani, N. Rega, G.A. Petersson, H. Nakatsuji, M. Hada, M. Ehara, K. Toyota, R. Fukuda, J. Hasegawa, M. Ishida, T. Nakajima, Y. Honda, O. Kitao, H. Nakai, M. Klene, X. Li, J.E. Knox, H.P. Hratchian, J.B. Cross, V. Bakken, C. Adamo, J. Jaramillo, R. Gomperts, R.E. Stratmann, O. Yazyev, A.J. Austin, R. Cammi, C. Pomelli, J.W. Ochterski, P.Y. Ayala, K. Morokuma, G.A. Voth, P. Salvador, J.J. Dannenberg, V.G. Zakrzewski, S. Dapprich, A.D. Daniels, M.C. Strain, O. Farkas, D.K. Malick, A.D. Rabuck, K. Raghavachari, J.B. Foresman, J.V. Ortiz, Q. Cui, A.G. Baboul, S. Clifford, J. Cioslowski, B.B. Stefanov, G. Liu, A. Liashenko, P. Piskorz, I. Komaromi, R.L. Martin, D.J. Fox, T. Keith, M.A. Al-Laham, C.Y. Peng, A. Nanayakkara, M. Challacombe, P.M.W. Gill, B. Johnson, W. Chen, M.W. Wong, C. Gonzalez, J.A. Pople, Gaussian 09, Revision E.01, Gaussian, Inc, Wallingford, CT, 2004.
[24] A.D. Becke, J. Chem. Phys. 98 (1993) 5648.
[25] M.H. Jamróz, Vibrational Energy Distribution Analysis VEDA 4, Warsaw, 2004.
[26] T. Lu, F. Chen, J. Comput. Chem. 33 (2012) 580–592.
[27] N.M. O'Boyle, A.L. Tenderholt, K.M. Langner, J. Comp. Chem. 29 (2008) 839–845.
[28] Michel F. Sanner, Python: a programming language for software integration and development, J. Mol. Graphics Mod. 17 (1991) 57–61.
[29] A.D. Bochevarov, E. Harder, T.F. Hughes, J.R. Greenwood, D.A. Braden, D.M. Philipp, D. Rinaldo, M.D. Halls, J. Zhang, R.A. Friesner, Jaguar: a high-performance quantum chemistry software program with strengths in life and materials sciences, Int. J. Quantum Chem. 113 (18) (2013) 2110–2142.
[30] Schrödinger Release 2018-1. 2018, , Jaguar, Schrödinger, LLC, New York, NY, 2018.
[31] L.D. Jacobson, A.D. Bochevarov, M.A. Watson, T.F. Hughes, D. Rinaldo, S. Ehrlich, T.B. Steinbrecher, S. Vaitheeswaran, D.M. Philipp, M.D. Halls, Automated transition state search and its application to diverse types of organic reactions, J. Chem. Theory Comput. 13 (11) (2017) 5780–5797.
[32] D. Shivakumar, J. Williams, Y. Wu, W. Damm, J. Shelley, W. Sherman, Prediction of absolute solvation free energies using molecular dynamics free energy perturbation and the OPLS force field, J. Chem. Theory Comput. 6 (5) (2010) 1509–1519.
[33] Z. Guo, U. Mohanty, J. Noehre, T.K. Sawyer, W. Sherman, G. Krilov, Probing the α-helical structural stability of stapled p53 peptides: molecular dynamics simulations and analysis, Chem. Biol. Drug Des. 75 (4) (2010) 348–359.
[34] K. J. Bowers, E. Chow, H. Xu, R. O. Dror, M. P. Eastwood, B. A. Gregersen, J. L. Klepeis, I. Kolossvary, M. A. Moraes, F. D. Sacerdoti. Scalable algorithms for molecular dynamics simulations on commodity clusters. in Proceedings of the 2006 ACM/IEEE Conference on Supercomputing. 2006. ACM.
[35] H.J. Berendsen, J.P. Postma, W.F. van Gunsteren, J. Hermans, Interaction models for water in relation to protein hydration, Intermolecular Forces, Springer 1981, pp. 331–342.
[36] Schrödinger Release 2018-1. vol. 2018, , Maestro, Schrödinger, LLC, New York, NY, 2018.
[37] A.D. Becke, Density-functional thermochemistry. III. The role of exact exchange, J. Chem. Phys. 98 (7) (1993) 5648–5652.
[38] E. Harder, W. Damm, J. Maple, C. Wu, M. Reboul, J.Y. Xiang, L. Wang, D. Lupyan, M.K. Dahlgren, J.L. Knight, OPLS3: a force field providing broad coverage of drug-like small molecules and proteins, J. Chem. Theory Comput. 12 (1) (2015) 281–296.
[39] W.L. Jorgensen, D.S. Maxwell, J. Tirado-Rives, Development and testing of the OPLS all-atom force field on conformational energetics and properties of organic liquids, J. Am. Chem. Soc. 118 (45) (1996) 11225–11236.
[40] W.L. Jorgensen, J. Tirado-Rives, The OPLS [optimized potentials for liquid simulations] potential functions for proteins, energy minimizations for crystals of cyclic peptides and crambin, J. Am. Chem. Soc. 110 (6) (1988) 1657–1666.
[41] Samina Alam, Sadaf Saeed, Andreas Fischer, Naeema Khana, Methyl 2 (2hydroxyacetamido) benzoate, Acta Cryst E66 (2010) 913.
[42] K. Swaminathan, U.C. Sinha, Structure of N-(o-carboxyphenyl) iminodiacetic acid, Acta Cryst C47 (1991) 119–121.
[43] M. Ladd, Introduction to Physical Chemistry, third ed. Cambridge University 393 Press, Cambridge, 1998.
[44] T. Engel, G. Drobny, P.J. Reid, Physical Chemistry for the Life Sciences, Pearson Prentice Hall, New York, NY, USA, 2008.
[45] M. Govindarajana, M. Karabacak, FT-IR, FT-Raman and UV spectral investigation; computed frequency estimation analysis and electronic structure calculations on 1-nitronaphthalene, Spectrochim. Acta A 85 (2012) 251–260.
[46] A.E. Reed, F. Weinhold, J. Chem. Phys. 78 (1983) 4066.
[47] F. Weinhold, Natural bond orbital methods, in: P.V.R. Schleyer, N.L. Allinger, T. Clark, J. Gasteiger, P.A. Kollman, I.I.I. H F Schaefer, P.R. Schreiner (Eds.), Encyclopedia of Computational Chemistry, vol. 3, John Wiley & Sons, Chichester 1998, p. 1792.
[48] F. Weinhold, C.R. Landis, Valency and Bonding: A Natural Bond Orbital Donor–Acceptor Perspective, Cambridge University Press, Cambridge, 2005.
[49] A.E. Reed, L.A. Curtis, F.A. Weinhold, Chem. Rev. 88 (1988) 899–926.
[50] J. Chocholousova, V. Vladimir Spirko, P. Hobza, Phys. Chem. Chem. Phys. 6 (2004) 37.

[51] G. Varsanyi, Vibrational Spectra of Benzene Derivatives, Academic Press, New York, NY, USA, 1969.
[52] B. Smith, Infrared Spectral Interpretation, a Systematic Approach, vol. 1, CRC Press, Washington, DC, 1999.
[53] N. Okulik, A.H. Jubert, Theoretical study on the structure and reactive sites of three non-steroidal anti-inflammatory drugs: ibuprofen, naproxen and tolmetin acids, J. Mol. Struct. THEOCHEM 769 (1) (2006) 135–141.
[54] J.S. Murray, J.M. Seminario, P. Politzer, P. Sjoberg, Average local ionization energies computed on the surfaces of some strained molecules, Int. J. Quantum Chem. 38 (S24) (1990) 645–653.
[55] P. Politzer, F. Abu-Awwad, J.S. Murray, Comparison of density functional and Hartree–Fock average local ionization energies on molecular surfaces, Int. J. Quantum Chem. 69 (4) (1998) 607–613.
[56] F.A. Bulat, A. Toro-Labbé, T. Brinck, J.S. Murray, P. Politzer, Quantitative analysis of molecular surfaces: areas, volumes, electrostatic potentials and average local ionization energies, J. Mol. Model. 16 (11) (2010) 1679–1691.
[57] J.A. War, K. Jalaja, Y.S. Mary, C.Y. Panicker, S. Armaković, S.J. Armaković, S.K. Srivastava, C. Van Alsenoy, Spectroscopic characterization of 1-[3-(1H-imidazol-1-yl) propyl]-3-phenylthiourea and assessment of reactive and optoelectronic properties employing DFT calculations and molecular dynamics simulations, J. Mol. Struct. 1129 (2017) 72–85.
[58] D.A. Zainuri, S. Arshad, N.C. Khalib, I.A. Razak, R.R. Pillai, S.F. Sulaiman, N.S. Hashim, K.L. Ooi, S. Armaković, S.J. Armaković, C.Y. Panicker, C. Van Alsenoy, Synthesis, XRD crystal structure, spectroscopic characterization (FT-IR, 1H and 13C NMR), DFT studies, chemical reactivity and bond dissociation energy studies using molecular dynamics simulations and evaluation of antimicrobial and antioxidant activities of a novel chalcone derivative, (E)-1-(4-bromophenyl)-3-(4-iodophenyl)prop-2-en-1-one, J. Mol. Struct. 1128 (2017) 520–533.
[59] V.V. Menon, E. Fazal, Y.S. Mary, C.Y. Panicker, S. Armaković, S.J. Armaković, S. Nagarajan, C. Van Alsenoy, FT-IR, FT-Raman and NMR characterization of 2-isopropyl-5-methylcyclohexyl quinoline-2-carboxylate and investigation of its reactive and optoelectronic properties by molecular dynamics simulations and DFT calculations, J. Mol. Struct. 1127 (2017) 124–137.
[60] S. Armaković, S.J. Armaković, S. Pelemiš, D. Mirjanić, Influence of sumanene modifications with boron and nitrogen atoms to its hydrogen adsorption properties, Phys. Chem. Chem. Phys. 18 (4) (2016) 2859–2870.
[61] P. Sjoberg, J.S. Murray, T. Brinck, P. Politzer, Average local ionization energies on the molecular surfaces of aromatic systems as guides to chemical reactivity, Can. J. Chem. 68 (8) (1990) 1440–1443.
[62] J.-T. Ye, L. Wang, H.-Q. Wang, Z.-Z. Chen, Y.-Q. Qiu, H.-M. Xie, Spirooxazine molecular switches with nonlinear optical responses as selective cation sensors, RSC Adv. 7 (2017) 642–650.
[63] C. Cassidy, J.M. Halbout, W. Donaldson, C.L. Tang, Nonlinear optical properties of urea, Opt. Commun. 29 (2) (1979) 243–247.
[64] P. Muthuraja, T. Shanmugavadivu, T. Joselin Beaula, V. Bena Jothy, M. Dhandapani, Influence of intramolecular hydrogen bonding interaction on the molecular properties of N-p-tolyl-5-oxo pyrrolidine-3-carboxylic acid: a theoretical and experimental study, Chem. Phys. Lett. 691 (2017) 114–121.
[65] S. Xavier, S. Periandy, Spectroscopic (FT-IR, FT-Raman, UV and NMR) investigation on 1-phenyl-2-nitropropene by quantum computational calculations, Spectrochim. Acta A Mol. Biomol. Spectrosc. 149 (2015) 216–230.
[66] R. Parthasarathi, Venkatraman Subramanian, Debesh R. Roy, P.K. Chattaraj, Electrophilicity index as a possible descriptor for biological activity, Bioorg. Med. Chem. 12 (21) (2004) 5533–5543.
[67] T. Lu, F. Chen, Quantitative analysis of molecular surface based on improved marching tetrahedra algorithm, J. Mol. Graphics Model. 38 (2012) 314–323.
[68] L. Tian, C. Feiwu, Calculation of Molecular Orbital Composition, 2011.
[69] Meng Xiao, T. Lu, Generalized charge decomposition analysis (GCDA) method, Journal of Advances in Physical Chemistry (4) (2015) 111–124.

[70] T. Le Bahers, C. Adamo, I. Ciofini, A qualitative index of spatial extent in charge transfer excitations, J. Chem. Theory Comput. 7 (2011) 2498–2506.
[71] Ciro A. Guido, Pietro Cortona, Benedetta Mennucci, Carlo Adamo, On the metric of charge transfer molecular excitations: a simple chemical descriptor, J. Chem. Theory Comput. 9 (7) (2013) 3118–3126.
[72] B. Smith, Infrared Spectral Interpretation, a Systematic Approach, CRC, Washington, DC, 1999.
[73] N.B. Colthup, L.H. Daly, S.E. Wiberley, Introduction to Infrared to and Raman Spectroscopy, Academic Press, New York, 1990.
[74] G. Socrates, Infrared and Raman Characteristic Group Frequencies, John Wiley & Sons Ltd, England, 1980.
[75] H. Endredi, F. Billes, S. Holly, Vibrational spectroscopic and quantum chemical study of the chlorine substitution of pyrazine, J. Mol. Struct. (THEOCHEM) 633 (2003) 73.
[76] C.P.D. Dwivedi, S.N. Sharma, Indian J. Pure Appl. Phys. 11 (1973) 447.
[77] H. Tanak, F. Ersahin, E. Agar, O. Buyukgungor, M. Yavuz, Anal. Sci. 24 (2008) 237.
[78] G. Chalasinski, M. Malgorzata and Szczesniak 1994 Chem. Rev.. 94 1723–1765.
[79] G. Varsanyi, Vibrational Spectra of Seven Hundred Benzene Derivatives Academic Press,
[80] A.J. Barnes, M.A. Majid, M.A. Stuckey, P. Gregory, C.V. Stead, Spectrochim. Acta A 41 (4) (1985) 629–635.
[81] N.P.G. Roeges, A Guide to the Complete Interpretation of Infrared Spectra of Organic Structures, Wiley, New York, 1994.
[82] A.D. Becke, K.E. Edgecombe, J. Chem. Phys. 92 (1990) 5397.
[83] H.L. Schmider, A.D. Becke, THEOCHEM J. Mol. Struct. 527 (2000) 51.
[84] H.L. Schmider, A.D. Becke, J. Chem. Phys. 116 (2002) 3184.
[85] T. Bitter, K. Ruedenberg, W.H.E. Schwarz, J. Comput. Chem. 28 (2007) 411.
[86] K. Ruedenberg, M.W. Schmidt, J. Comput. Chem. 28 (2007) 391.
[87] E. Matito, M. Sola, Coord. Chem. Rev. 253 (2009) 647.
[88] R.J. Gillespie, J. Chem. Educ. 40 (1963) 295.
[89] Andreas Savin, Reinhard Nesper, Steffen Wengert, Thomas E. Fassler, ELF: the electron localization function, Angew. Chem. In. Ed. Engl. 36 (1997) 1808–1832.
[90] Heiko Jacobsen, Can. J. Chem. 86 (2008) 695.
[91] T. Andersson, A. Broo, E. Evertsson, Prediction of drug candidates' sensitivity toward autoxidation: computational estimation of C-H dissociation energies of carbon-centered radicals, J. Pharm. Sci. 103 (7) (2014) 1949–1955 2014.
[92] S.W. Hovorka, C. Schöneich, Oxidative degradation of pharmaceuticals: theory, mechanisms and inhibition, J. Pharm. Sci. 90 (3) (2001) 253–269.
[93] J.S. Wright, H. Shadnia, L.L. Chepelev, Stability of carbon-centered radicals: effect of functional groups on the energetics of addition of molecular oxygen, J. Comput. Chem. 30 (7) (2009) 1016–1026.
[94] G. Gryn'ova, J.L. Hodgson, M.L. Coote, Revising the mechanism of polymer autooxidation, Organic & biomolecular chemistry 9 (2) (2011) 480–490.
[95] C.A. Lipinski, F. Lombardo, B.W. Dominy, P.J. Feeney, Experimental and computational approaches to estimate solubility and permeability in drug discovery and development settings, Adv. Drug Deliv. Rev. 23 (1–3) (1997) 3–25.
[96] C.A. Lipinski, Lead-and drug-like compounds: the rule-of-five revolution, Drug Discov. Today Technol. 1 (4) (2004) 337–341.
[97] M. Congreve, R. Carr, C. Murray, H. Jhoti, A 'rule of three' for fragment-based lead discovery? Drug Discov. Today 8 (19) (2003) 876–877.
[98] A.K. Ghose, V.N. Viswanadhan, J.J. Wendoloski, A knowledge-based approach in designing combinatorial or medicinal chemistry libraries for drug discovery. 1. A qualitative and quantitative characterization of known drug databases, J. Comb. Chem. 1 (1) (1999) 55–68.
[99] Roman Aleksander Laskowski, M.W. Macarthur, D.S. Moss, Janet Thornton, PROCHECK: a program to check the stereochemical quality of protein structures, J. Appl. Crystallogr. 26 (2) (1993) 283–291.